

Nonthermal electron and ion acceleration by magnetic reconnection in large laser-driven plasmas

S. R. Titorica^{a)}

*High Energy Density Science Division, SLAC National Accelerator Laboratory,
Menlo Park, California 94025, USA*

*Kavli Institute for Particle Astrophysics and Cosmology, Stanford University,
Stanford, California 94025, USA*

*Department of Astrophysical Sciences, Princeton University, Princeton,
New Jersey 08544, USA and*

*International Research Collaboration Center, National Institute of Natural Sciences,
Tokyo 105-0001, Japan*

M. Hoshino

*Department of Earth and Planetary Science, University of Tokyo, Tokyo 113-0033,
Japan*

T. Abel

*Kavli Institute for Particle Astrophysics and Cosmology, Stanford University,
Stanford, California 94025, USA*

*Department of Physics, Stanford University, Stanford, California 94305,
USA and*

*SLAC National Accelerator Laboratory, Menlo Park, California 94025,
USA*

F. Fiuza^{b)}

*High Energy Density Science Division, SLAC National Accelerator Laboratory,
Menlo Park, California 94025, USA*

(Dated: 7 December 2020)

Magnetic reconnection is a fundamental plasma process that is thought to play a key role in the production of nonthermal particles associated with explosive phenomena in space physics and astrophysics. Experiments at high-energy-density facilities are starting to probe the microphysics of reconnection at high Lundquist numbers and large system sizes. We have performed particle-in-cell (PIC) simulations to explore particle acceleration for parameters relevant to laser-driven reconnection experiments. We study particle acceleration in large system sizes that may be produced soon with the most energetic laser drivers available, such as at the National Ignition Facility. In these conditions, we show the possibility of reaching the multi-plasmoid regime, where plasmoid acceleration becomes dominant. Our results show the transition from X point to plasmoid-dominated acceleration associated with the merging and contraction of plasmoids that further extend the maximum energy of the power-law tail of the particle distribution for electrons. We also find for the first time a system-size-dependent emergence of nonthermal ion acceleration in driven reconnection, where the magnetization of ions at sufficiently large sizes allows them to be contained by the magnetic field and energized by direct X point acceleration. For feasible experimental conditions, electrons and ions can attain energies of $\epsilon_{max,e}/k_B T_e > 100$ and $\epsilon_{max,i}/k_B T_i > 1000$. Using PIC simulations with binary Monte Carlo Coulomb collisions we study the impact of collisionality on plasmoid formation and particle acceleration. The implications of these results for understanding the role reconnection plays in accelerating particles in space physics and astrophysics are discussed.

^{a)}Electronic mail: totorica@princeton.edu

^{b)}Electronic mail: fiuza@slac.stanford.edu

I. INTRODUCTION

Magnetic reconnection is a fundamental plasma process that converts magnetic field energy into plasma flows, heating, and energetic particles¹. It is believed to play an important role in the dynamics of magnetized plasmas in a wide range of scenarios in space physics, astrophysics, and laboratory nuclear fusion devices²⁻⁴. One aspect of reconnection that is of particular interest is its ability to produce energetic particles with nonthermal distributions, which are directly measured in association with reconnection in the Earth's magnetosphere⁵⁻⁷ and inferred to be present in magnetized astrophysical objects from radiation spectra⁸. The complex multi-scale dynamics involved in reconnection and particle acceleration in realistic systems make it a challenge to fully understand the particle acceleration properties of reconnection, and this is currently an active area of research.

Energetic laser facilities, including the Gekko XII laser at Osaka University, the OMEGA laser at the University of Rochester, and the National Ignition Facility (NIF) at Lawrence Livermore National Laboratory, can focus kJ to MJ energies onto sub-millimeter spot sizes over nanosecond time scales and create high-energy-density plasma states in the laboratory. These lasers can ablate plasmas with keV temperatures and ~ 1000 km/s flows when focused onto solid targets, potentially reaching regimes where collisional mean free paths exceed the system size. In sufficiently collisionless regimes, the governing equations can be shown to be invariant to scaling transformations^{9,10} that open the possibility of using these experiments to gain insight into the reconnection dynamics occurring in systems in space physics and astrophysics¹¹.

Over the past decade there has been significant effort and progress in developing laser-driven plasma experiments into a platform for studying the dynamics of reconnection in a controlled laboratory setting¹²⁻²³. By focusing kilojoule per nanosecond lasers onto solid targets, expanding plasma plumes are ablated, and reconnection can occur between self-generated Biermann battery²⁴⁻²⁷ fields or externally imposed magnetic fields¹⁸. These experiments are in an interesting regime with strongly driven flows, large system sizes in terms of the microscopic scales, and the potential to reach relativistic regimes²⁸. The plasma properties and electromagnetic fields in these experiments can be measured using diagnostics including proton radiography, Thompson scattering, and shadowgraphy. Past experiments have measured features of reconnection including changes in magnetic field topology¹³,

plasma heating¹⁷, and the formation of plasma jets¹², however it is challenging to access the full details of the kinetic physics occurring in these systems with current diagnostics and several important aspects, including nonthermal particle acceleration, are not yet fully understood.

In previous work by several of us, we have used fully kinetic particle-in-cell (PIC) simulations to model laser-driven plasma experiments and found the possibility of nonthermal electron acceleration for the conditions and geometries of recently performed experiments^{29,30}. For these conditions we found through particle tracking studies that the electrons are energized primarily by direct acceleration at the X points, with plasmoid related acceleration contributing only minor additional energy gain. Numerical studies by other groups have shown similar electron acceleration^{31–33}. Here we extend our study to larger system sizes in terms of the microscopic ion skin depth $d_i = c/\omega_{pi}$, which could be produced at megajoule class laser facilities such as NIF. Recent laboratory astrophysics experiments on NIF focused on the study of particle acceleration in collisionless shocks have demonstrated the generation of large collisionless plasmas with $L/d_i > 500$ for the system size³⁴. NIF experiments on magnetic reconnection are also underway and recent measurements have suggested fast reconnection in a thin and elongated current sheet³⁵. As the characteristic length scale of plasmoid formation is on the order of the ion skin depth d_i , system sizes of $L/d_i > 100$ are expected to reach a regime where many plasmoids are present in the current sheet, potentially merging to larger scales and introducing new particle acceleration channels. We present below simulation results for such system sizes. We find in our simulations that multi-plasmoid dynamics enhance electron acceleration, and we observe for the first time a system-size-dependent emergence of nonthermal ion acceleration in strongly driven systems for sufficiently large sizes. In the context of laser-driven reconnection experiments, this is the first time that nonthermal ion acceleration has been observed. Experiments in this regime would be valuable to benchmark numerical simulations in well-controlled conditions and would further extend our understanding of the role reconnection plays in accelerating particles in space and astrophysics, which are often expected to be in the multi-plasmoid regime².

The outline of this manuscript is as follows. The details of the numerical simulations are given in Section II. We investigate the acceleration of electrons in Section III and the acceleration of ions in Section IV, extending our previous studies to larger system sizes. In

Section V we study the influence of particle collisionality using collisional simulations. In Section VI we discuss these results and their implications for reconnection in space physics and astrophysics, and in Section VII we summarize our conclusions.

II. DESCRIPTION OF SIMULATIONS

To model the microphysics of laser-driven reconnection experiments we use two-dimensional PIC simulations performed with the fully relativistic, massively parallel, state-of-the-art PIC code OSIRIS^{36–39}. PIC simulations represent the plasma by a finite number of discrete simulation particles that interact through self-consistent electromagnetic fields⁴⁰, and can capture the full kinetic physics of highly nonlinear plasma systems. We use both standard collisionless PIC simulations as well as simulations with Coulomb collisions taken into account through the use of a binary Monte Carlo collision operator⁴¹. The simulations are initialized at a time partway through the experiment, when the two magnetized plasma bubbles are expanding and about to interact. These generic initial conditions can be connected to experimental geometries including both self-generated and externally imposed magnetic fields⁴², and have been used in previous PIC studies that have given insight into laser-driven reconnection^{29,30,43–46}. The centers of the plasma bubbles are given by the vectors $\mathbf{R}^{(1)} = (0, R, 0)$ and $\mathbf{R}^{(2)} = (0, -R, 0)$, and the corresponding radial vectors from the bubble centers are $\mathbf{r}^{(i)} = \mathbf{r} - \mathbf{R}^{(i)}$, where R is the radius of each bubble when they begin to interact. The initial density profile is given by $n_b + n^{(1)} + n^{(2)}$ where $n^{(i)}(r^{(i)}) = (n_0 - n_b) \cos^2\left(\frac{\pi r^{(i)}}{2R}\right)$ if $r^{(i)} < R$, 0 otherwise. Here, $n_b = 0.01n_0$ is the background plasma density. The initial velocity profile is given by $\mathbf{V}^{(1)} + \mathbf{V}^{(2)}$ where $\mathbf{V}^{(i)}(r^{(i)}) = V_0 \sin\left(\frac{\pi r^{(i)}}{R}\right) \mathbf{r}^{(i)}$ if $r^{(i)} < R$, 0 otherwise. The initial magnetic field corresponds to the sum of two oppositely aligned ribbons of finite flux, $\mathbf{B}^{(1)} + \mathbf{B}^{(2)}$ where $\mathbf{B}^{(i)}(r^{(i)}) = B_0 \sin\left(\frac{\pi(R-r^{(i)})}{2L_B}\right) \hat{\phi}^{(i)}$ if $R - 2L_B \leq r^{(i)} \leq R$, 0 otherwise. Here $L_B = R/4$ is the initial half-width of the magnetic field ribbon. The initial electric field is $\mathbf{E} = -\mathbf{V} \times \mathbf{B}/c$, consistent with the initial motion of the magnetized plasma. An initial out-of-plane current J_z is included that is consistent with $\nabla \times \mathbf{B} = \frac{4\pi}{c} \mathbf{J}$ and distributed to the electrons and ions by the inverse of their mass ratio. In this study we use both systems that are uniform and periodic along the direction of the reconnection outflows, as well as finite systems with circular plasma bubbles, extending our previous work to larger systems sizes in terms of the ion skin depth (Figure 1). The periodic systems allow

us to study very large system sizes, and use the same initial conditions as described above but with the radial vectors changed to $\mathbf{r}^{(1)} = (0, y - R, 0)$ and $\mathbf{r}^{(2)} = (0, y + R, 0)$. These simulations have square domains with the length of each side ranging from $L/d_i \simeq 53 - 212$. The finite sized circular bubble systems allow the inclusion of the effects of particle escape and for these we use bubble radii ranging from $R/d_i \simeq 26.5 - 106$. The anti-symmetry of these systems allows the use of periodic boundaries along the inflow (y) direction. Periodic boundaries are also used along the x axis, and for the finite sized systems the domain is set to be 8 times the bubble radius along this axis to prevent recirculation of the reconnection outflows.

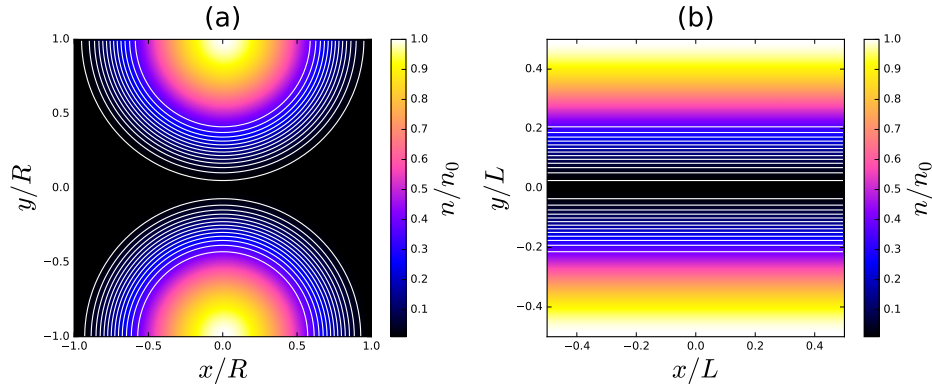


FIG. 1. Density with overlaid magnetic fields lines (white) for the initial conditions of the finite (a) and infinite (b) systems. The finite system simulations have domains of $8R \times 2R$ with bubble radius R ranging from $R/d_i \simeq 26.5 - 106$. The infinite systems have square domains of side length L ranging from $L/d_i \simeq 53 - 212$.

We directly match many of the plasma parameters to their values estimated from experimental measurements⁴⁴. For the Alfvénic and sonic Mach numbers we model a range of $M_A = V_0/V_A = 4 - 16$ and $M_S = V_0/C_S = 2$, where $V_A = B_0/\sqrt{4\pi n_0 m_i}$ is the Alfvén speed and $C_S = \sqrt{Z T_e/m_i}$ is the sound speed. For the electron plasma beta this corresponds to $\beta_e = n_0 T_e/(B_0^2/8\pi) = 2(M_A/M_S)^2 = 8 - 32$. The initial temperatures T_e and T_i are taken to be equal and uniform throughout the plasma. To make the simulations computationally feasible we do not match the experimental values for the parameters C_S/c and $m_i/m_e Z$ (where c is the speed of light, m_i and m_e the ion and electron masses, and Z the ion charge). For these parameters we use $V_0/c = 0.1$ and $m_i/m_e Z = 128$, with C_S chosen to correctly match M_S . This is a commonly used approximation that effectively reduces the speed

of light and increases the electron mass, but can still allow for an adequate separation of the relevant temporal and spatial scales to accurately model the physical processes^{32,44,47,48}. This will primarily impact the electron-scale physics and electromagnetic waves which are not the focus of this study, and we have performed convergence tests to ensure this choice of numerical parameters is not obscuring the physical processes³⁰. For the numerical parameters of the simulations, the discrete timestep is $\Delta t = 0.35 \omega_{pe}^{-1}$, and the resolution of the spatial grid is $\Delta x = 0.5c/\omega_{pe} \simeq 0.04c/\omega_{pi}$. Cubic interpolation is used to weigh between the particle and field quantities, and 64 particles per cell per species are used in the initial conditions.

III. ELECTRON ACCELERATION

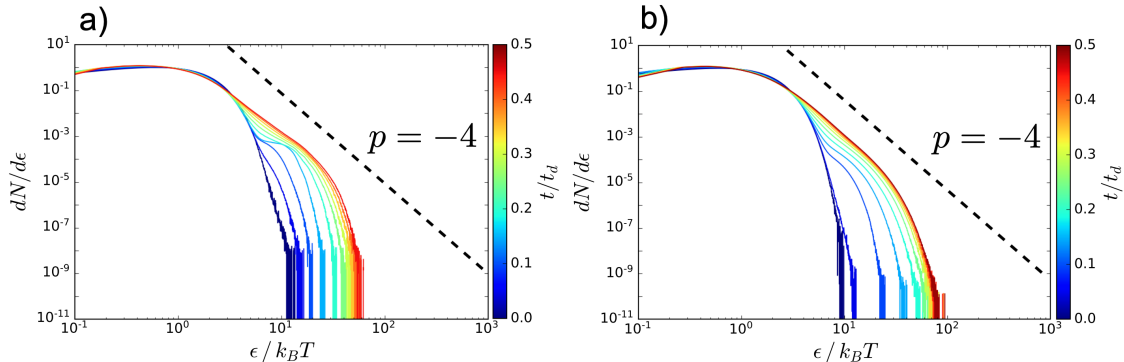


FIG. 2. Temporal evolution of the electron energy spectra for two different system sizes: (a) $L/d_i = 53$ and (b) $L/d_i = 212$. The colored lines show the evolution of the spectra from $t/t_d = 0$ to $t/t_d = 0.5$ at equally spaced time intervals. A power-law spectrum with index $p = -4$ is plotted for reference.

We first discuss the details of electron acceleration, extending our previous work^{29,30} to larger system sizes. Figures 2 (a) and (b) show the temporal evolution of the electron spectra for systems with lengths along the reconnection outflow direction (x) of $L/d_i = 53$ and $L/d_i = 212$, respectively. The plots show the temporal evolution of the spectra from $t/t_d = 0$ to $t/t_d = 0.5$, where $t_d = R/V_0$ is the relevant timescale for the interaction and the experimental measurements. Both systems are periodic in the x -direction and form plasmoids in the current sheet. The system shown in (b) is scaled four times larger along

each dimension compared to the system shown in (a), and thus also advects four times the amount of magnetic flux into the current sheet. This allows reconnection to proceed for longer, leading to plasmoids growing and merging which has important consequences for the particle acceleration. The spectra in both cases are very similar, with a power-law index of approximately $p = -4$. Both the value of this index and the relative insensitivity of the spectrum to system size are consistent with recent measurements in the context of reconnection in Earth's magnetotail⁴⁹. The energy contained above 5 (10) times the thermal energy is approximately 10 (2) percent of the total energy of the electrons for the system with $L/d_i = 212$.

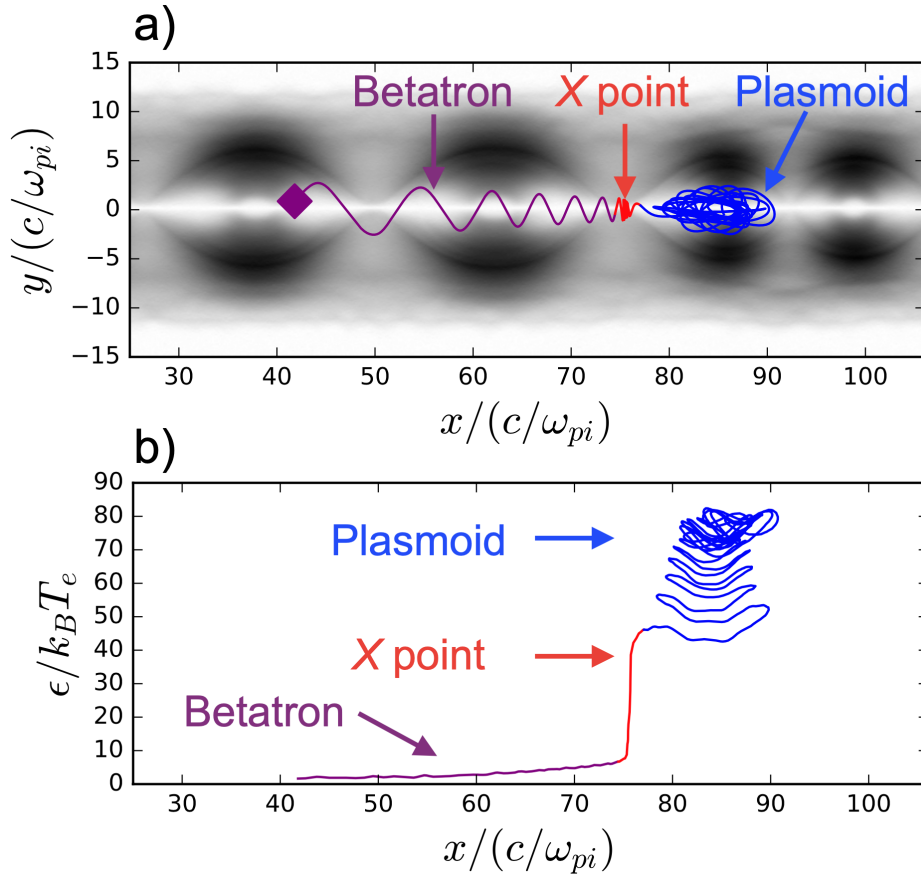


FIG. 3. (a) Trajectory of a representative energetic electron from the $L/d_i = 212$ simulation plotted over the magnitude of the in-plane magnetic field, with its initial position indicated by the diamond. (b) Energy of the electron as a function of its position along the x axis. The trajectories show the three different phases to the acceleration, distinguished by different colors.

Figure 3 shows an example trajectory of an energetic electron from the simulation with

$L/d_i = 212$, highlighting the importance of energy gain inside the plasmoid. Figure 3 (a) shows the trajectory of the electron in space, plotted over the magnitude of the magnetic field in a zoomed in region at a time when several plasmoids have formed. Figure 3 (b) shows the energy of the electron as a function of its position along the x -axis, revealing three distinct phases to the acceleration. The purple segment of the particle trajectory shows the initial phase of betatron acceleration. At early times the magnetic field is compressed from the colliding magnetized plasma flows, and the magnetized electron gains a small amount of energy from adiabatic betatron acceleration. The electron then gains a large amount of energy in a localized region along x , which can be identified as the location of a reconnection X point in the magnetic field profile. Here the magnetic field vanishes, and the electron is non-adiabatically accelerated by the out-of-plane electric field associated with reconnection. The in-plane magnetic field then deflects the electron away from the X point and into the plasmoid, where it becomes trapped. As new magnetic flux is added onto the plasmoid from reconnection and the plasmoid contracts, the electron gains an amount of energy that is comparable to that gained at the X point.

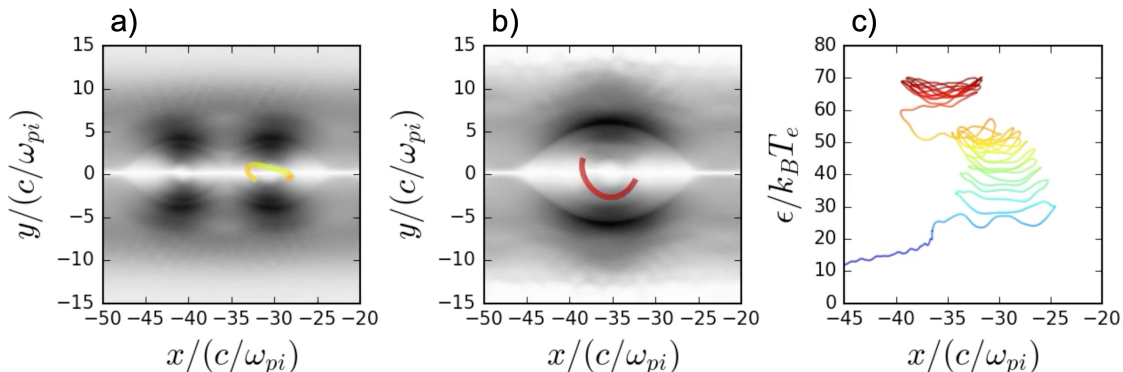


FIG. 4. Magnitude of the magnetic field from the $L/d_i = 212$ simulation (a) before and (b) after the plasmoid merger, with segments of the trajectory of an energetic electron, colored by its energy according to (c). (c) Shows the energy of the electron as a function of its position along the x axis.

In addition to acceleration inside a single contracting plasmoid, plasmoid mergers are seen to frequently occur in this system and further energize particles. Figure 4 shows an example trajectory of an electron from the $L/d_i = 212$ simulation, colored by its energy, before (a) and after (b) the merging of two plasmoids. Figure 4 (c) shows the electron's energy as a function of its position along the x -axis. The electron initially is trapped inside a single plasmoid

and gains energy as it contracts. When the two plasmoids merge together, the electron experiences a fast increase in energy as it is reflected from the edge of the newly merged larger plasmoid. This larger plasmoid then continues to contract and further energizes the electron. Acceleration associated with contracting⁴⁷ and merging^{50,51} plasmoids has been studied in past simulations and is of strong interest for explaining the efficient acceleration of electrons and power-law energy spectra associated with reconnection in space physics and astrophysics. In both cases the acceleration mechanism can be interpreted as the result of Fermi Type B reflections⁵² from the magnetic field at the edge of the plasmoids. The restriction of these simulations to two spatial dimensions makes the plasmoids effectively uniform in the out-of-plane dimension. In three-dimensional systems plasmoids may be unstable to the drift-kink instability which has wave-vector components in the out-of-plane dimension. However this instability is typically strongly suppressed over the timescales of the reconnection dynamics at realistic mass ratios⁵³, and past work has found that the particle acceleration can remain effective even in the absence of coherent plasmoids⁵⁴. The periodic boundaries along the outflow direction in these simulations may enhance the frequency of plasmoid mergers by preventing plasmoids from escaping the system. However, because the simulations are run for less than one Alfvén crossing time the artificial effects of the boundaries on plasmoid evolution and particle acceleration are limited, and nonthermal electron acceleration and plasmoid merging are seen to persist in the simulations of finite systems.

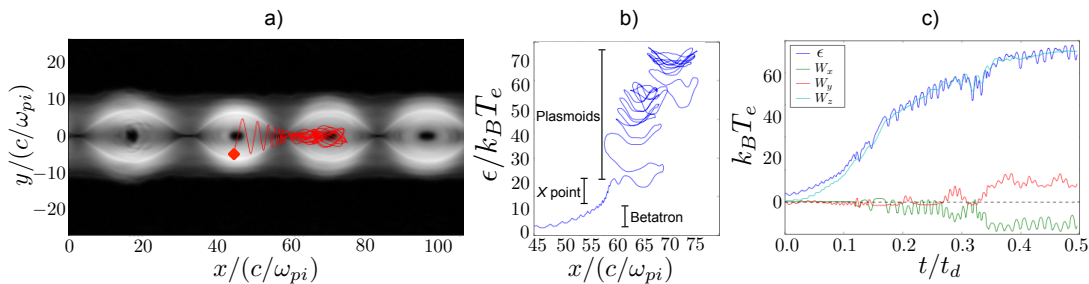


FIG. 5. (a) Trajectory of an energetic electron plotted over the magnitude of the magnetic field from the $L/d_i = 212$ simulation. (b) Energy of the electron as a function of position along the x -axis. (c) Total energy of the electron and work point done by the individual electric field components as a function of time.

The energy gain for the processes of betatron acceleration, direct X point acceleration,

and plasmoid contraction and merging comes from the out-of-plane component of the electric field. Figure 5 (a) shows the trajectory of another representative energetic electron from the $L/d_i = 212$ simulation. From the plot of energy as a function of position along the x axis in Figure 5 (b), it can be seen that this electron experiences betatron acceleration, X point acceleration, and acceleration from plasmoid contraction and a plasmoid merging event. The total energy of the particle and the work done by the three components of the electric field are shown in Figure 5 (c), showing how the work done on the electron primarily comes from the force from the out-of-plane electric field. The energetic electron tracks we have analyzed show that the energy gain from betatron acceleration is typically minor compared to that from the X point and plasmoids. Direct acceleration by the reconnection electric field at the X points usually provides the first significant gain of energy, with the remaining coming from plasmoid contraction and merging. The overall energy gain from plasmoid contraction and merging is typically comparable to or greater than that from the X points. At even larger system sizes where plasmoids evolve over longer timescales we expect the contribution of plasmoid related particle acceleration to become increasingly dominant, as the X points contribute primarily to the initial phase of acceleration.

IV. ION ACCELERATION

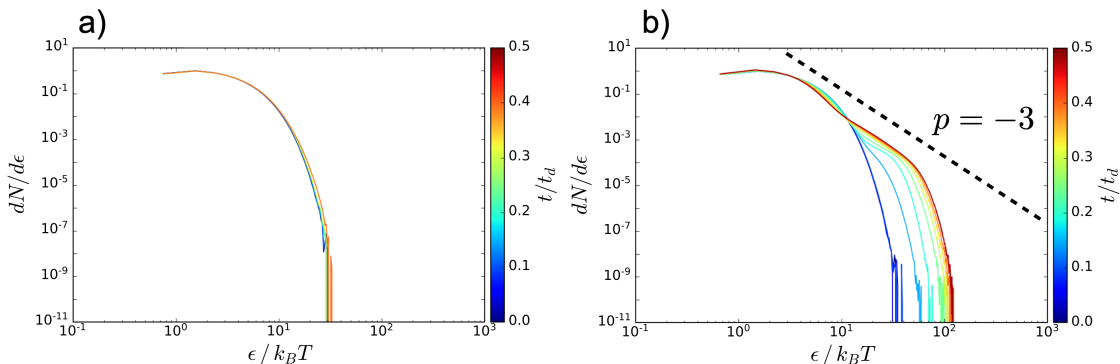


FIG. 6. Temporal evolution of the ion energy spectra for two different system sizes: (a) $L/d_i = 53$ and (b) $L/d_i = 212$. The colored lines show the evolution of the spectra from $t/t_d = 0$ to $t/t_d = 0.5$ at equally spaced time intervals. The nonthermal component that develops for the larger system size resembles a power-law with an index of approximately $p = -3$ (plotted for reference).

The ions exhibit a dramatic change in behavior as the system size is increased. Figure 6 shows the temporal evolution of the ion spectra for a system size of $L/d_i = 53$ in (a) and $L/d_i = 212$ in (b). For the small system size, the ions show only a small amount of heating and remain well described by a Maxwellian. For the large system size, the ions gain a significant amount of energy and exhibit the clear development of a nonthermal tail in their spectra, extending to more than 100 times the initial thermal energy. This difference is due to the ability of the magnetic field to magnetize the ions. At the small system size, the amount of magnetic flux is not sufficient to contain the ions, and the ions pass through the interaction region before they can be energized by reconnection related acceleration mechanisms. At the large system size, however, ions are magnetized and can be contained inside the reconnection region, allowing them to spend a significant amount of time in the reconnection layer and become energized by reconnection. The energization is seen to saturate at later times due to the finite amount of plasma and magnetic flux in the system. The system is initialized with plasma flows with a finite velocity that drive reconnection, however because no new plasma or magnetic flux are introduced the reconnection dynamics are strongest during the initial interaction and become weaker at later times as the system relaxes. Similar to what was seen for the electrons, the nonthermal component that develops has a shape resembling a power-law, in this case with an index of approximately $p = -3$. The value of this index and the strong influence of the system size on the spectrum are also consistent with recent satellite measurements of reconnection in Earth's magnetotail⁴⁹. The energy contained above 5 (10) times the thermal energy is approximately 30 (10) percent of the total energy of the ions for the system with $L/d_i = 212$.

Figure 7 shows an example evolution of an ion that is energized by reconnection in the $L/d_i = 212$ simulation. The ion's trajectory in space is plotted over the magnitude of the magnetic field in Figure 7 (a), showing how it is contained in the current sheet by the magnetic field and repeatedly passes through a reconnection X point. The ion's energy as a function of its position along the y axis is shown in Figure 7 (b), showing how it initially gains energy from betatron acceleration during two reflections as the magnetic field is compressed. Once reconnection has initiated, the ion gains energy from the reconnection electric field as it crosses over the X point. Figure 7 (c) shows the total energy of the ion and the work done by the electric field components, showing how it is again the out-of-plane component of the electric field that provides the energy. For this system size, the Larmor radii of the

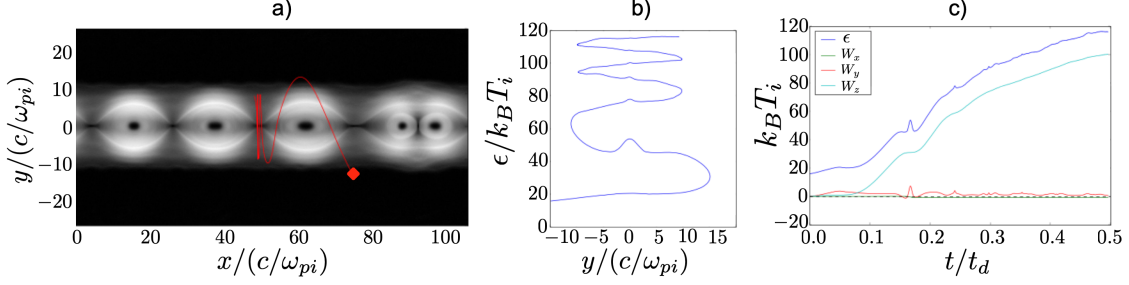


FIG. 7. (a) Trajectory of an energetic ion plotted over the magnitude of the magnetic field from the $L/d_i = 212$ simulation. (b) Energy of the ion as a function of position along the y -axis. (c) Total energy of the ion and work done by the individual electric field components as a function of time.

ions are still too large compared to the size of the plasmoids to be energized in plasmoid related particle acceleration mechanisms.

The previous simulations were for systems that were periodic along the direction of the reconnection outflows, which means particles can not escape as they do in more realistic finite systems. Figure 8 shows the ion spectra for several simulations with finite system sizes, demonstrating how the ion acceleration persists in an open configuration. Figure 8 (a) shows a comparison for system sizes of $R/d_i = 27, 53,$ and 133 , showing the emergence of ion acceleration as the system size is increased and the additional magnetic flux allows the ions to be contained in the reconnection layer. Figure 8 (b) shows the large system size, $R/d_i = 133$, for three different magnetic field strengths. The finite number of constant width energy bins used to calculate these spectra can lead to a loss of resolution at the low energy end, however the high energy features of interest are well resolved. The maximum energy increases with the initial magnetic field, consistent with the ions gaining energy from reconnection when the magnetic flux contained is sufficient to contain the ions. As the magnetic field strength increases by a factor of 2, the high energy cutoff of the distribution increases by ≈ 1.5 . This is reduced from the linear increase that would result from a reconnection rate and reconnection electric field that scale linearly with the initial magnetic field, which is expected for collisionless reconnection⁵⁵, due to the effects of flux pileup from the driven flows which enhances the strength of the magnetic field in the reconnection layer. The local magnetic field is then stronger than the initial magnetic field in the flows,

and this enhancement is more effective at higher Alfvénic Mach numbers. Figure 8 (a) compares systems with different sizes, while Figure 8 (b) compares systems with different initial magnetic fields. However, as V_0 is held constant, in both cases the spectra extend to higher energies as the amount of initial magnetic flux in the system increases. The similarity of the shape and maximum energy of the spectra for cases with similar amounts of initial flux shows the importance of having a sufficient amount of flux for containing ions in the reconnection layer and allowing them to be energized by the reconnection electric field.

The finite size of the system in the out-of-plane dimension L_z (which is not modeled in the 2D simulations) acts to limit the acceleration of the particles. The maximum energy obtainable from the reconnection electric field can be estimated by the work done by this field, $\epsilon_{max} = qEL_z$, where L_z is the length of the system along the direction of the reconnection electric field. This was taken into account in our previous work to estimate the maximum energy gain of an electron in terms of the initial plasma conditions²⁹, which can be extended for ions of arbitrary Z and T_i/T_e as $\epsilon_{max}/k_B T_i = (1/2)(ZT_e/T_i)(M_S^2/M_A)(L_z/d_i)$. In terms of the particle gyroradius based on the inflow velocity, $\rho_0 = V_0/(qB_0/mc)$, this can be written as $\epsilon_{max} = 2mV_0^2 L_z/\rho_0$. Using the diameter of the plasma bubbles for L_z , $T_e = T_i$, and $Z = 1$ to compare with our simulations, this estimate agrees reasonably well with the cutoffs of the power-law spectra as shown by the dotted lines in Figure 8. Particle tracking of ions and electrons from the simulation with $L/d_i = 212$ showed that the most energetic particles travel an out-of-plane distance of $\sim 200 - 300 d_i$ by the end of the simulation, comparable to the system size. While this maximum energy estimate was derived assuming X point acceleration, analyzing the energy as a function of position along the out-of-plane direction for energetic particles in our particle tracking shows that it is also a reasonable estimate when plasmoids are contributing significantly to the energization. We have previously studied the angular dependence of energetic electron acceleration in these experiments in detail and found that the electrons escape the system in a fan-like profile³⁰. Ions and electrons are accelerated by the reconnection electric field in opposite directions due to the signs of their charges, and this contrast could be a powerful experimental signature for identifying particles that are accelerated by reconnection.

Recent reconnection experiments on NIF³⁵ using self-generated magnetic fields produced a long ($\sim 100 d_i$) current sheet along the direction of the reconnection outflows, however the smaller size ($\sim 10 d_i$) along the direction of the reconnection electric field limited the

potential for particle acceleration. For these conditions our maximum energy estimate gives $\epsilon_{max}/T_e \sim 3$ for electrons, which closely agrees with the ratio of the estimated integrated reconnection electric field (based on the measured reconnected flux and experimental timescale) to the electron temperature predicted by simulations designed to match the experiments. Measurements and simulations of the self-generated magnetic fields in similar systems²⁶ suggest that the magnetic field is limited to a region above the target that is significantly shorter than the separation between the centers of the plasma bubbles, indicating that this configuration is likely not ideal for studying particle acceleration. The use of a well-controlled external magnetic field, such as used in recent experiments¹⁸, provides in principle a more suitable experimental configuration where the magnetized plasma region has an out-of-plane size that is comparable to the size of the plasma bubbles. Assuming the alternative geometry of counter-streaming flows³⁴ and an externally imposed field of 10-30 T (producible using a magneto-inertial fusion electrical discharge system (MIFEDS)⁵⁶) significantly enhances the potential for particle acceleration. For this case it should be possible to have system sizes $L_z/d_i > 200$ in the direction of the reconnection electric field, producing maximum ion energies of $\epsilon_{max,i}/T_i > 1000$ and electron energies of $\epsilon_{max,e}/T_e > 100$. Choosing configurations that maximize the energies attainable by particles in terms of the initial thermal energy has the advantage of extending the power-law portion of the energy spectrum, which will help for identifying this feature in experimental measurements and precisely defining the spectral index.

V. COLLISIONAL EFFECTS

Recent experimental measurements of magnetic reconnection using laser-driven plasmas with self-generated magnetic fields did not show evidence of plasmoid formation, and it has been argued that these results contradict the expectations from previous simulations^{19,44}. However, these experiments were done in a regime where the collisional mean free paths are comparable to the length scales in the system, and most previous PIC simulations considered a collisionless plasma. It is thus important to understand how the collisionality affects plasmoid formation and particle acceleration in laser-driven reconnection. Collisional effects can be included in PIC simulations using a binary Monte Carlo Coulomb collision operator⁴¹. We investigate the role of collisional effects in these systems using PIC simu-

lations of expanding, magnetized plasma bubbles with varied levels of collisionality. The Lundquist number, $S = LV_A/\eta = (L/d_i)\omega_{ce}\tau_e$, gives the ratio of the characteristic timescale of the magnetic field dynamics to that of resistive diffusion. Another important parameter for considering the collisional physics in reconnection is the electron mean free path in terms of the ion skin depth λ/d_i , as d_i is the characteristic length scale of plasmoid formation. This parameter is related to the Lundquist number as $S = (L/d_i)(2/\beta_e)^{1/2}(m_i/m_e Z)^{1/2}(\lambda/d_i)$. Our simulations match the system size in terms of the ion skin depth L/d_i and the electron plasma beta β_e to the experimental values, however an artificially reduced mass ratio of $m_i/m_e Z = 128$ is used. This expression for the Lundquist number makes it evident that when β_e and L/d_i are matched to the experimental values but an artificial mass ratio is used, it is not possible to simultaneously match S and λ/d_i to the experimental values. It remains to be determined which parameter, S or λ/d_i , is more important to match to accurately capture the dynamics of the physical system with a reduced mass ratio simulation.

We parameterize the collisionality in the system using the electron collisional mean free path in terms of the ion skin depth. Figure 9 shows the magnitude of the magnetic field in four simulations with the same initial conditions ($R_{bubble}/(c/\omega_{pi}) = 27$, $M_S = 2$, $M_A = 4$) but varied levels of collisionality, showing changes in the structure of the current sheet as the collisionality changes. By varying the electron mean free path in terms of the ion skin depth, we see a clear suppression of plasmoid formation as this ratio drops below one. Typical conditions for experiments with self-generated fields are below this threshold for plasmoid formation ($\lambda/d_i \approx 0.5$), and thus our results suggest that the discrepancy between previous simulations and experiments may be due to collisional effects. Previous simulations have matched S and found plasmoid formation in a regime where experiments did not observe plasmoids^{19,57}. Instead, in our simulations we match λ/d_i , and show that this dimensionless parameter controls the suppression of plasmoid formation as observed in recent experiments - providing support for this approach of scaling the reduced mass ratio simulations. Experiments using externally imposed fields¹⁸ can produce more collisionless regimes that are above the threshold for plasmoid formation ($\lambda/d_i > 10$), and are likely the ideal configuration for studying particle acceleration and plasmoid dynamics.

Figure 10 shows an investigation of the effects of collisionality on the particle acceleration for simulations with $R_{bubble}/(c/\omega_{pi}) = 27$, $M_S = 2$, $M_A = 4$. Figures 10 (a) and (b) show the magnetic field magnitude and electron spectra for a collisionless simulation, and

Figures 10 (c) and (d) show the same quantities for a collisional simulation. The collisional simulation has $\lambda/d_i = 0.1$, which is in a regime where plasmoid formation is suppressed and the reconnection electric field strength is below the Dreicer field, limiting the efficiency of X point acceleration. The red lines in Figures 10 (b) and (d) show the spectra just outside the reconnection layer and the blue lines show the spectra inside the reconnection layer (integrated over the regions indicated by the red and blue rectangles in Figures 10 (a) and (c)). In both cases electrons are accelerated by the reconnection electric field at X points, however in the collisional case the electrons are also heated by collisions with ions, which only slightly changes the shape of the spectrum. The similarity of these spectra indicates that at these smaller system sizes the acceleration from plasmoids is not a dominant energization mechanism, which is consistent with the findings in our previous studies^{29,30}. We expect the differences in the electron spectrum to become significant at larger system sizes such as the $> 100d_i$ systems studied above where significant plasmoid mediated particle acceleration occurs in the collisionless case but would be suppressed in the collisional case.

VI. DISCUSSION

Within the heliosphere, plasmoids can be observed directly, for example in solar flares in the solar corona⁵⁸ and substorms in the Earth's magnetotail^{59,60}. They are believed to have important effects on aspects such as the reconnection rate, energy transport, and nonthermal particle acceleration. Simulations for relevant conditions have shown the acceleration of nonthermal populations of particles, but have not conclusively determined the shape of the resulting spectra and how they depend on the plasma conditions^{47,50,61-63}. In highly magnetized astrophysical objects, it is expected that the reconnection conditions can reach the relativistic regime, where the magnetic energy per particle exceeds the rest mass energy ($\sigma = B^2/4\pi nmc^2$). Although reconnecting current sheets cannot be directly observed for these objects, simulations for the expected conditions show the importance of plasmoids^{54,64}. Plasmoids are particularly important for particle acceleration, where they provide the dominant energization mechanism contributing to the power-law distributions of particles that are produced. In the trans-relativistic regime of $\sigma \sim 1$, relevant for accretion flows in black holes, nonthermal particle acceleration can occur for both electron and ions⁶⁵. While the conditions in these systems are very different from those of the experiments modeled in this

study, the qualitative features of the acceleration are similar, including contributions from both X points and plasmoids. The results of this study show that laser-driven plasma experiments at large system sizes could allow the study of reconnection in the multi-plasmoid regime in a laboratory setting that would allow for controlled plasma conditions and tuning between different regimes of reconnection. Such experiments would be valuable for developing and benchmarking models of multi-plasmoid reconnection and particle acceleration that could be connected to systems in both space physics and astrophysics, due to the similarity of the physics involved and the scalability of the governing equations.

The acceleration of ions from reconnection is an important topic that has been investigated in systems ranging from astrophysics to the laboratory^{66–74}. A critical new finding in this study is the emergence of ion acceleration at sufficiently large laser-driven system sizes. These results are important for systems in space physics which often feature simultaneous electron and ion acceleration associated with reconnection events. A particularly promising connection can be made between these experiments and reconnection in Earth’s magnetotail. Nonthermal electrons and ions are commonly produced in association with reconnection in the magnetotail, however there are many unsolved problems about their production. How the reconnection conditions impact the acceleration efficiency and the relative partitioning of the dissipated magnetic energy, and why sometimes only one of the two species experiences significant energization are aspects that are not yet well understood^{75,76}. Laser-driven plasma experiments capable of measuring both electron and ion acceleration by magnetic reconnection as a function of the plasma parameters would allow a better understanding of the similarities and differences between the acceleration of electrons and ions. A recent study analyzed satellite observations in the magnetotail to determine what conditions are favorable for ion acceleration and found that the spatial system size and reconnection electric field strength are critical factors for producing energetic ions⁴⁹, which is directly in accordance with the results presented above.

Additionally, the conditions in the Earth’s magnetotail current sheet are in many ways remarkably similar to those typical of laser-driven plasma experiments, with characteristic ion temperatures of \sim keV, electron temperatures of several hundred eV, Alfvén speed of \sim 1000 km/s, and normalized system sizes on the order of hundreds of ion skin depths. The moderate system sizes characteristic of the magnetotail and laser-driven plasmas are unique compared to those in solar physics and astrophysics because they are large enough

to feature complex coupling between global and microscopic scales, yet still feasible to be modeled using fully kinetic simulations. Studies of these systems could be used for developing global models of reconnection that could potentially be extrapolated to the larger system sizes characteristic of solar physics and astrophysics. Further exploration of the promising synergy between reconnection in laser-driven plasmas and the Earth's magnetotail will be the subject of future work.

VII. CONCLUSION

In conclusion, using fully kinetic PIC simulations, we have modeled laser-driven plasma experiments for the conditions of future experiments at megajoule class laser facilities such as the National Ignition Facility. At large system sizes, the multi-plasmoid regime can be reached, where many plasmoids are present simultaneously in the current sheet and merge to larger scales. Plasmoid related acceleration processes enhance the efficiency of electron acceleration and the maximum energies that can be attained. For systems with sufficient flux to trap ions in the reconnection layer, we find the emergence of nonthermal ion acceleration associated with energy gain from the reconnection electric field at the X points. Furthermore, using collisional PIC simulations, we find that collisional effects can suppress plasmoid formation, and thus need to be carefully considered in the planning of experiments and numerical modeling. These results show that laser-driven plasmas at large system sizes offer a powerful platform for studying nonthermal electron and ion acceleration by reconnection and the interplay between these processes in systems in space physics and astrophysics.

ACKNOWLEDGMENTS

This work was supported by the U.S. Department of Energy SLAC Contract No. DE-AC02-76SF00515 and by the U.S. DOE Early Career Research Program under FWP 100331. The authors acknowledge the OSIRIS Consortium, consisting of UCLA and IST (Portugal) for the use of the OSIRIS 3.0 framework and the visXD framework. S. T. was also supported by the NASA Jack Eddy Postdoctoral Fellowship (NNH15ZDA001N-LWS). Simulations were run on Mira (ALCF supported under Contract No. DE-AC02-06CH1135) through an IN-

CITE award, on Blue Waters, and on the Bullet Cluster at SLAC.

DATA AVAILABILITY

The data that support the findings of this study are available from the corresponding author upon reasonable request.

REFERENCES

- ¹E. G. Zweibel and M. Yamada, *Annual Review of Astronomy and Astrophysics* **47**, 291 (2009).
- ²H. Ji and W. Daughton, *Physics of Plasmas* **18**, 111207 (2011), arXiv:1109.0756.
- ³A. S. Joglekar, A. G. R. Thomas, W. Fox, and A. Bhattacharjee, *Physical Review Letters* **112**, 1 (2014), arXiv:1507.03629v1.
- ⁴J. B. Taylor, *Reviews of Modern Physics* **58**, 741 (1986).
- ⁵E. Moebius, M. Scholer, D. Hovestadt, and G. Paschmann, *Journal of Geophysical Research* **88**, 7742 (1983).
- ⁶M. Øieroset, R. P. Lin, T. D. Phan, D. E. Larson, and S. D. Bale, *Physical Review Letters* **89**, 1 (2002).
- ⁷S. Imada, M. Hoshino, and T. Mukai, *Geophysical Research Letters* **32**, 1 (2005).
- ⁸M. Hoshino and Y. Lyubarsky, *Space Science Reviews* **173**, 521 (2012).
- ⁹D. D. Ryutov, R. P. Drake, and B. A. Remington, *The Astrophysical Journal Supplement Series* **127**, 465 (2000).
- ¹⁰D. D. Ryutov, N. L. Kugland, H. S. Park, C. Plechaty, B. A. Remington, and J. S. Ross, *Plasma Physics and Controlled Fusion* **54**, 105021 (2012).
- ¹¹B. A. Remington, R. P. Drake, and D. D. Ryutov, *Reviews of Modern Physics* **78**, 755 (2006).
- ¹²P. M. Nilson, L. Willingale, M. C. Kaluza, C. Kamperidis, S. Minardi, M. S. Wei, P. Fernandes, M. Notley, S. Bandyopadhyay, M. Sherlock, R. J. Kingham, M. Tatarakis, Z. Najmudin, W. Rozmus, R. G. Evans, M. G. Haines, A. E. Dangor, and K. Krushelnick, *Physical Review Letters* **97**, 1 (2006).

- ¹³C. K. Li, F. H. Séguin, J. A. Frenje, J. R. Rygg, R. D. Petrasso, R. P. Town, O. L. Landen, J. P. Knauer, and V. A. Smalyuk, *Physical Review Letters* **99**, 055001 (2007).
- ¹⁴P. M. Nilson, L. Willingale, M. C. Kaluza, C. Kamperidis, S. Minardi, M. S. Wei, P. Fernandes, M. Notley, S. Bandyopadhyay, M. Sherlock, R. J. Kingham, M. Tatarakis, Z. Najmudin, W. Rozmus, R. G. Evans, M. G. Haines, A. E. Dangor, and K. Krushelnick, *Physics of Plasmas* **15**, 092701 (2008).
- ¹⁵L. Willingale, P. M. Nilson, M. C. Kaluza, A. E. Dangor, R. G. Evans, P. Fernandes, M. G. Haines, C. Kamperidis, R. J. Kingham, C. P. Ridgers, M. Sherlock, A. G. R. Thomas, M. S. Wei, Z. Najmudin, K. Krushelnick, S. Bandyopadhyay, M. Notley, S. Minardi, M. Tatarakis, and W. Rozmus, *Physics of Plasmas* **17**, 043104 (2010).
- ¹⁶J. Zhong, Y. Li, X. Wang, J. Wang, Q. Dong, C. Xiao, S. Wang, X. Liu, L. Zhang, L. An, F. Wang, J. Zhu, Y. Gu, X. He, G. Zhao, and J. Zhang, *Nature Physics* **6**, 984 (2010).
- ¹⁷Q. L. Dong, S. J. Wang, Q. M. Lu, C. Huang, D. W. Yuan, X. Liu, X. X. Lin, Y. T. Li, H. G. Wei, J. Y. Zhong, J. R. Shi, S. E. Jiang, Y. K. Ding, B. B. Jiang, K. Du, X. T. He, M. Y. Yu, C. S. Liu, S. Wang, Y. J. Tang, J. Q. Zhu, G. Zhao, Z. M. Sheng, and J. Zhang, *Physical Review Letters* **108**, 1 (2012), arXiv:1203.4036v1.
- ¹⁸G. Fiksel, W. Fox, A. Bhattacharjee, D. H. Barnak, P.-Y. Chang, K. Germaschewski, S. X. Hu, and P. M. Nilson, *Physical Review Letters* **113**, 1 (2014).
- ¹⁹M. J. Rosenberg, C. K. Li, W. Fox, A. B. Zylstra, C. Stoeckl, F. H. Séguin, J. A. Frenje, and R. D. Petrasso, *Physical Review Letters* **114**, 1 (2015).
- ²⁰M. J. Rosenberg, C. K. Li, W. Fox, I. Igumenshchev, F. H. Séguin, R. P. Town, J. A. Frenje, C. Stoeckl, V. Glebov, and R. D. Petrasso, *Nature Communications* **6**, 6190 (2015).
- ²¹X. X. Pei, J. Y. Zhong, Y. Sakawa, Z. Zhang, K. Zhang, H. G. Wei, Y. T. Li, Y. F. Li, B. J. Zhu, T. Sano, Y. Hara, S. Kondo, S. Fujioka, G. Y. Liang, F. L. Wang, and G. Zhao, *Physics of Plasmas* **23**, 032125 (2016).
- ²²Y. Kuramitsu, T. Moritaka, Y. Sakawa, T. Morita, T. Sano, M. Koenig, C. D. Gregory, N. Woolsey, K. Tomita, H. Takabe, Y. L. Liu, S. H. Chen, S. Matsukiyo, and M. Hoshino, *Nature Communications* **9**, 5109 (2018).
- ²³T. Morita, K. Nagashima, M. Edamoto, K. Tomita, T. Sano, Y. Itadani, R. Kumar, M. Ota, S. Egashira, R. Yamazaki, S. J. Tanaka, S. Tomita, S. Tomiya, H. Toda, I. Miyata, S. Kakuchi, S. Sei, N. Ishizaka, S. Matsukiyo, Y. Kuramitsu, Y. Ohira, M. Hoshino, and Y. Sakawa, *Physics of Plasmas* **26**, 090702 (2019), arXiv:1909.02880.

- ²⁴M. Haines, *Physical Review Letters* **78**, 254 (1997).
- ²⁵J. A. Stamper, *Laser and Particle Beams* **9**, 841 (1991).
- ²⁶L. Gao, P. M. Nilson, I. V. Igumenshchev, M. G. Haines, D. H. Froula, R. Betti, and D. D. Meyerhofer, *Physical Review Letters* **114**, 1 (2015).
- ²⁷J. Matteucci, W. Fox, A. Bhattacharjee, D. B. Schaeffer, C. Moissard, K. Germaschewski, G. Fiksel, and S. X. Hu, *Physical Review Letters* **121**, 1 (2018).
- ²⁸A. E. Raymond, C. F. Dong, A. McKelvey, C. Zulick, N. Alexander, A. Bhattacharjee, P. T. Campbell, H. Chen, V. Chvykov, E. Del Rio, P. Fitzsimmons, W. Fox, B. Hou, A. Maksimchuk, C. Mileham, J. Nees, P. M. Nilson, C. Stoeckl, A. G. Thomas, M. S. Wei, V. Yanovsky, K. Krushelnick, and L. Willingale, *Physical Review E* **98**, 1 (2018).
- ²⁹S. R. Titorica, T. Abel, and F. Fiuza, *Physical Review Letters* **116**, 1 (2016), arXiv:1601.05845.
- ³⁰S. R. Titorica, T. Abel, and F. Fiuza, *Physics of Plasmas* **24**, 041408 (2017).
- ³¹W. Fox, J. Park, W. Deng, G. Fiksel, A. Spitkovsky, and A. Bhattacharjee, *Physics of Plasmas* **24**, 092901 (2017).
- ³²K. Huang, Q. Lu, C. Huang, Q. Dong, H. Wang, F. Fan, Z. Sheng, S. Wang, and J. Zhang, *Physics of Plasmas* **24**, 102101 (2017).
- ³³K. Huang, Q. Lu, L. Gao, H. Ji, X. Wang, and F. Fan, *Physics of Plasmas* **25**, 052104 (2018).
- ³⁴F. Fiuza, G. F. Swadling, A. Grassi, H. G. Rinderknecht, D. P. Higginson, D. D. Ryutov, C. Bruulsema, R. P. Drake, S. Funk, S. Glenzer, G. Gregori, C. K. Li, B. B. Pollock, B. A. Remington, J. S. Ross, W. Rozmus, Y. Sakawa, A. Spitkovsky, S. Wilks, and H.-S. Park, *Nature Physics* (2020), 10.1038/s41567-020-0919-4.
- ³⁵W. Fox, D. B. Schaeffer, M. J. Rosenberg, G. Fiksel, J. Matteucci, H. S. Park, A. F. A. Bott, K. Lezhnin, A. Bhattacharjee, D. Kalantar, B. A. Remington, D. Uzdensky, C. K. Li, F. H. Séguin, and S. X. Hu, arXiv (2020), arXiv:2003.06351.
- ³⁶R. G. Hemker, arXiv (2015), arXiv:1503.00276.
- ³⁷R. A. Fonseca, L. O. Silva, F. S. Tsung, V. K. Decyk, W. Lu, C. Ren, W. B. Mori, S. Deng, S. Lee, T. Katsouleas, and J. C. Adam, *Lect. Notes Comput. Sci.* **2331**, 342 (2002).
- ³⁸R. A. Fonseca, S. F. Martins, L. O. Silva, J. W. Tonge, F. S. Tsung, and W. B. Mori, *Plasma Physics and Controlled Fusion* **50**, 124034 (2008), arXiv:0810.2460.

- ³⁹R. A. Fonseca, J. Vieira, F. Fiuza, A. Davidson, F. S. Tsung, W. B. Mori, and L. O. Silva, *Plasma Physics and Controlled Fusion* **55**, 124011 (2013), arXiv:1310.0930.
- ⁴⁰J. M. Dawson, *Reviews of Modern Physics* **55**, 403 (1983).
- ⁴¹T. Takizuka and H. Abe, *Journal of Computational Physics* **25**, 205 (1977).
- ⁴²D. D. Ryutov, N. L. Kugland, M. C. Levy, C. Plechaty, J. S. Ross, and H. S. Park, *Physics of Plasmas* **20**, 032703 (2013).
- ⁴³W. Fox, A. Bhattacharjee, and K. Germaschewski, *Physical Review Letters* **106**, 1 (2011), arXiv:1104.0605.
- ⁴⁴W. Fox, A. Bhattacharjee, and K. Germaschewski, *Physics of Plasmas* **19**, 056309 (2012).
- ⁴⁵S. Lu, Q. Lu, Q. Dong, C. Huang, S. Wang, J. Zhu, Z. Sheng, and J. Zhang, *Physics of Plasmas* **20**, 112110 (2013).
- ⁴⁶S. Lu, Q. Lu, C. Huang, Q. Dong, J. Zhu, Z. Sheng, S. Wang, and J. Zhang, *New Journal of Physics* **16**, 083021 (2014).
- ⁴⁷J. F. Drake, M. Swisdak, H. Che, and M. A. Shay, *Nature* **443**, 553 (2006).
- ⁴⁸X. Li, F. Guo, and H. Li, *The Astrophysical Journal* **879**, 5 (2019).
- ⁴⁹S. Imada, M. Hirai, and M. Hoshino, *Earth, Planets and Space* **67**, 203 (2015).
- ⁵⁰M. Oka, T.-D. Phan, S. Krucker, M. Fujimoto, and I. Shinohara, *The Astrophysical Journal* **714**, 915 (2010), arXiv:1004.1154.
- ⁵¹A. Le, H. Karimabadi, J. Egedal, V. Roytershteyn, and W. Daughton, *Physics of Plasmas* **19**, 072120 (2012).
- ⁵²E. Fermi, *Physical Review* **75**, 1169 (1949), arXiv:0707.2783v2.
- ⁵³W. Daughton, *Physics of Plasmas* **6**, 1329 (1999).
- ⁵⁴F. Guo, H. Li, W. Daughton, and Y. H. Liu, *Physical Review Letters* **113**, 1 (2014), arXiv:1405.4040.
- ⁵⁵P. L. Pritchett, *Journal of Geophysical Research: Space Physics* **106**, 3783 (2001).
- ⁵⁶G. Fiksel, R. Backhus, D. H. Barnak, P. Y. Chang, J. R. Davies, D. Jacobs-Perkins, P. McNally, R. B. Spielman, E. Vigas, and R. Betti, *Review of Scientific Instruments* **89**, 084703 (2018).
- ⁵⁷K. V. Lezhnin, W. Fox, J. Matteucci, D. B. Schaeffer, A. Bhattacharjee, M. J. Rosenberg, and K. Germaschewski, *Physics of Plasmas* **25**, 093105 (2018), arXiv:1806.05289.
- ⁵⁸S. Takasao, A. Asai, H. Isobe, and K. Shibata, *The Astrophysical Journal* **828**, 103 (2016), arXiv:1611.00108.

- ⁵⁹A. Ieda, S. Machida, T. Mukai, Y. Saito, T. Yamamoto, A. Nishida, T. Terasawa, and S. Kokubun, *Journal of Geophysical Research: Space Physics* **103**, 4453 (1998).
- ⁶⁰L. J. Chen, A. Bhattacharjee, P. A. Puhl-Quinn, H. Yang, N. Bessho, S. Imada, S. Mühlbachler, P. W. Daly, B. Lefebvre, Y. Khotyaintsev, A. Vaivads, A. Fazakerley, and E. Georgescu, *Nature Physics* **4**, 19 (2008).
- ⁶¹X. R. Fu, Q. M. Lu, and S. Wang, *Physics of Plasmas* **13**, 012309 (2006).
- ⁶²M. Hoshino, T. Mukai, T. Terasawa, and I. Shinohara, *Journal of Geophysical Research* **106**, 25979 (2001).
- ⁶³J. T. Dahlin, J. F. Drake, and M. Swisdak, *Physics of Plasmas* **21**, 092304 (2014), arXiv:1406.0831.
- ⁶⁴L. Sironi and A. Spitkovsky, *The Astrophysical Journal* **783**, L21 (2014), arXiv:1401.5471.
- ⁶⁵D. Ball, L. Sironi, and F. Özel, *The Astrophysical Journal* **862**, 80 (2018), arXiv:1803.05556.
- ⁶⁶J. F. Drake, M. Swisdak, T. D. Phan, P. A. Cassak, M. A. Shay, S. T. Lepri, R. P. Lin, E. Quataert, and T. H. Zurbuchen, *Journal of Geophysical Research: Space Physics* **114**, 1 (2009).
- ⁶⁷J. F. Drake, M. Opher, M. Swisdak, and J. N. Chamoun, *The Astrophysical Journal* **709**, 963 (2010).
- ⁶⁸K. M. Schoeffler, J. F. Drake, M. Swisdak, and K. Knizhnik, *Astrophysical Journal* **764**, 126 (2013).
- ⁶⁹F. Guo, X. Li, H. Li, W. Daughton, B. Zhang, N. Lloyd-Ronning, Y.-H. Liu, H. Zhang, and W. Deng, *The Astrophysical Journal* **818**, L9 (2016).
- ⁷⁰E. Cazzola, D. Curreli, S. Markidis, and G. Lapenta, *Physics of Plasmas* **23**, 112108 (2016), arXiv:1610.09104.
- ⁷¹X. Li, F. Guo, H. Li, and G. Li, *The Astrophysical Journal* **843**, 21 (2017).
- ⁷²R. Jarvinen, R. Vainio, M. Palmroth, L. Juusola, S. Hoilijoki, Y. Pfau-Kempf, U. Ganse, L. Turc, and S. Vonalfthan, *Geophysical Research Letters* **45**, 1723 (2018).
- ⁷³K. G. McClements, J. O. Allen, S. C. Chapman, R. O. Dendy, S. W. Irvine, O. Marshall, D. Robb, M. Turnyanskiy, and R. G. Vann, *Plasma Physics and Controlled Fusion* **60**, 025013 (2018).
- ⁷⁴L. Vlahos and H. Isliker, *Plasma Physics and Controlled Fusion* **61**, 014020 (2019).

⁷⁵S. Imada, M. Hirai, M. Hoshino, and T. Mukai, *Journal of Geophysical Research: Space Physics* **116**, 1 (2011).

⁷⁶M. Hoshino, *The Astrophysical Journal* **868**, L18 (2018).

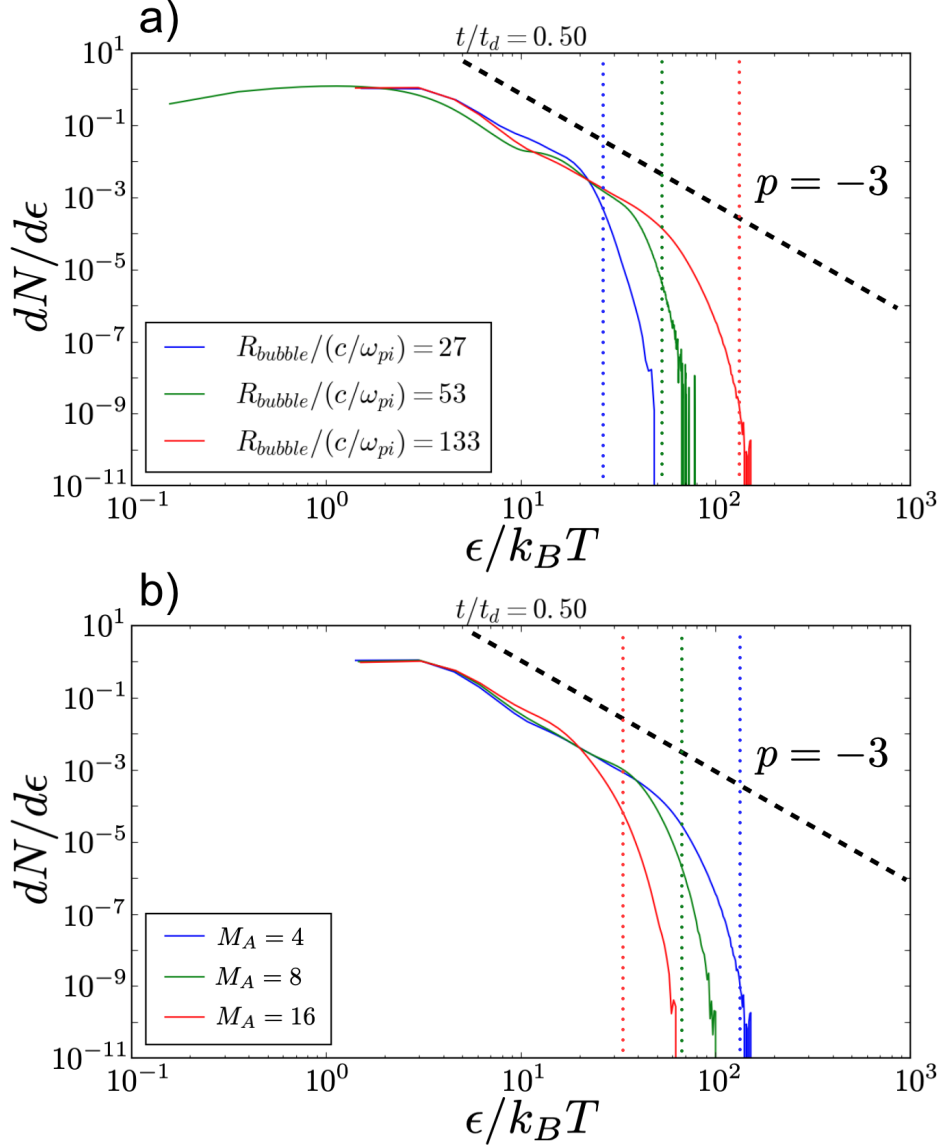


FIG. 8. (a) Ion spectra for finite system simulations with sizes of $R/d_i = 27, 53$, and 133 . (b) Ion spectra with $R/d_i = 133$ for three different initial magnetic field strengths, parameterized by the Alfvénic Mach number M_A . Blue: $M_A = 4$ (same strength as the spectra in (a)), green: $M_A = 8$, and red: $M_A = 16$. A power-law spectrum with index $p = -3$ is plotted for reference. Dotted lines show the maximum energy estimate from the formula in the text for the spectrum of the corresponding color.

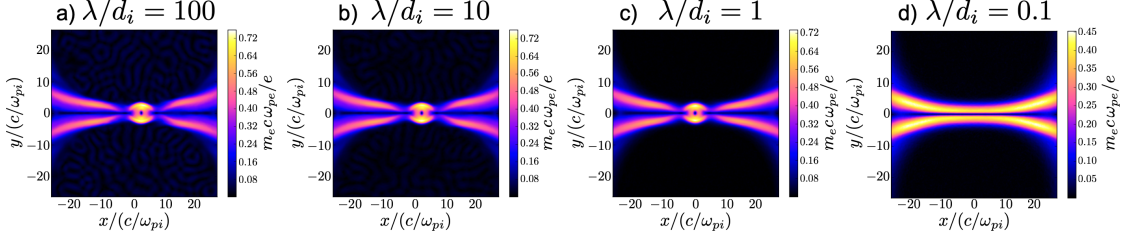


FIG. 9. Magnetic field magnitude for four simulations with the same initial conditions ($R_{bubble}/(c/\omega_{pi}) = 27$, $M_S = 2$, $M_A = 4$) but varied levels of collisionality, parameterized by the electron mean free path in terms of the ion skin depth d_i . Color scales are adjusted for each simulation to highlight the structural features of the current sheet. (a) $\lambda/d_i = 100$, (b) $\lambda/d_i = 10$, (c) $\lambda/d_i = 1$, (d) $\lambda/d_i = 0.1$.

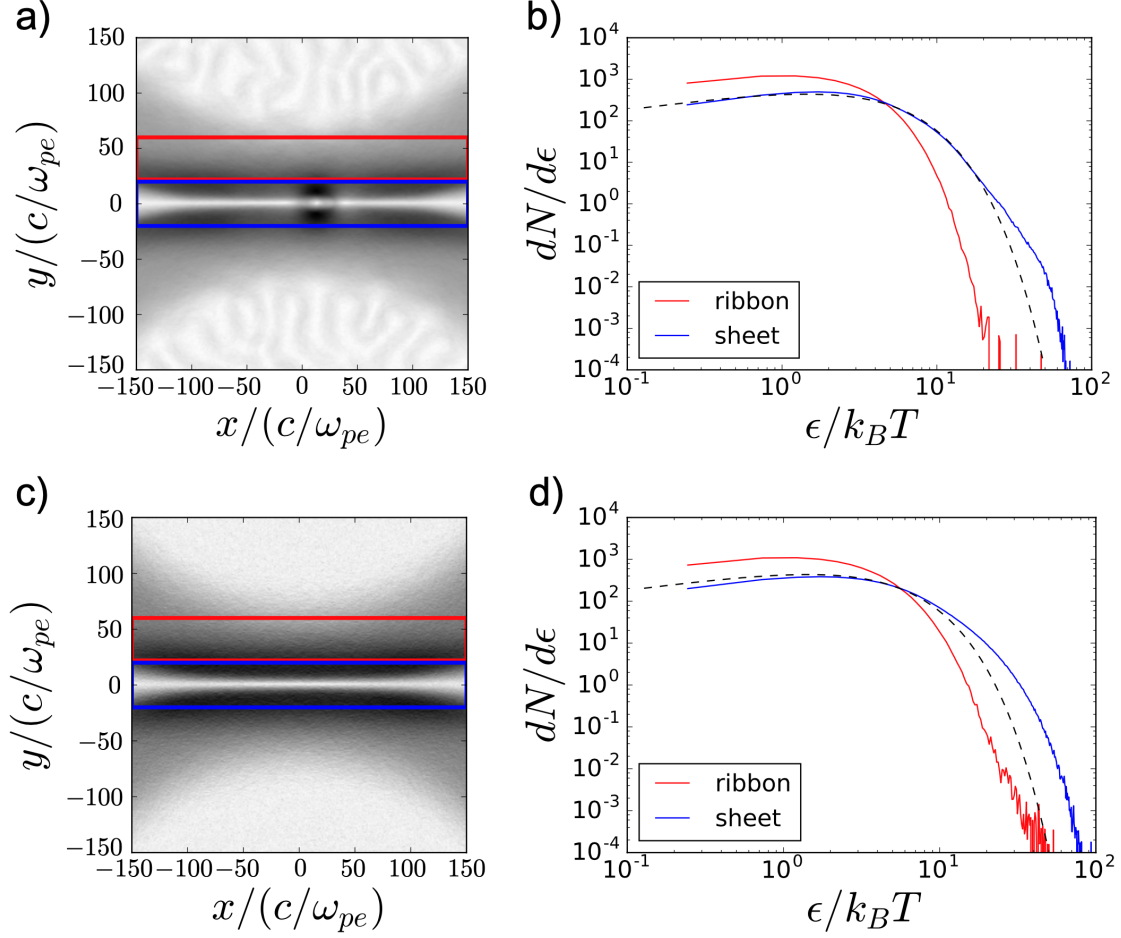


FIG. 10. Magnetic field magnitude for a collisionless simulation (a) and a collisional simulation with $\lambda/d_i = 0.1$ (c). (b) and (d) show the electron spectra in the regions indicated by the boxes in (a) and (c), respectively. Dashed lines show a Maxwell-Boltzmann distribution with the same average energy as the spectrum inside the current sheet for the collisionless simulation. Both simulations are initialized with $R_{bubble}/(c/\omega_{pi}) = 27$, $M_S = 2$, and $M_A = 4$.